CrossMark

Advances in the study of nano-structured Co/MCM-41 materials: surface and magnetic characterization

Verónica R. Elías[1] · Natalia I. Cuello[1] · Leandro Andrini[2] · Félix G. Requejo[2] · Marcos I. Oliva[3] · Griselda A. Eimer[1]

Abstract Co-modified mesoporous supports with MCM-41 structure and several metal loadings were successfully synthesized by a fast wet impregnation method. The nature and location of different Co species formed on the solids were inferred by TEM/SEM, XPS, XANES/EXAFS, adsorption of pyridine coupled to FT-IR spectroscopy and temperature dependence of magnetization. The presence of Co oxide species (clusters and Co_3O_4 nanoparticles) inside the channels of all the samples could be evidenced by TEM, XPS and XANES/EXAFS. In this sense, the surface Co/Si atomic ratios obtained by XPS were notably lower than the corresponding bulk Co/Si ratios obtained by ICP, indicating that the Co atoms are mostly incorporated inside the mesopores channels of the silica matrix. Nevertheless, by TEM, Co_3O_4 nanoparticles of small size segregated on the external surface of the silicate were also observed for the higher metal loadings. The temperature dependence of the magnetization performed for the Co/M(2.5) sample allowed to assign its superparamagnetic behavior to the presence of clusters and Co_3O_4 nanoparticles of very small size that grow inside the MCM-41 mesopores. Therefore, the analyses presented in this work indicate that a Co theoretical loading of 2.5 wt% leads to the formation of Co oxide nanospecies in the MCM-41 support with a particular superparamagnetic behavior. This sample with improved structural and magnetic properties result an attractive porous solid for drug hosting, to be applied in the field of the controlled release of medicaments.

Keywords EXAFS/XANES · Magnetic properties · XPS · Surface properties

✉ Griselda A. Eimer
geimer@frc.utn.edu.ar

Verónica R. Elías
veroelias@gmail.com

1 Centro de Investigación y Tecnología Química (CITeQ) (UTN-CONICET), Facultad Regional Córdoba, Maestro López y Cruz Roja Argentina, Ciudad Universitaria, 5016 Córdoba, Argentina

2 Instituto de Física de La Plata, CCT La Plata, CONICET-Dpto de Física, Fac. Cs. Exactas, Universidad Nacional de La Plata, La Plata, Argentina

3 IFEG-CONICET -FaMAF-Universidad Nacional de Córdoba, Córdoba, Argentina

1 Introduction

Mesoporous molecular sieves modified with metal oxides have different applications such as supports for gas sensors, electrode materials for batteries, supercapacitors, fuels cells, sorbents for separation, media for gas storage and drug delivery [1–6]. In this sense, Co is one of the transition metals extensively studied for their interesting properties. Regarding the novel applications, Co oxide has showed a good electrochemical performance in terms of specific capacity and cyclability [7] and nanosized Co_3O_4 has exhibited high capacitance as electrode in supercapacitors. Moreover, supported Co oxides on mesoporous materials are of wide interest for their known applications in several areas. Thus, they have been used as catalysts for the Fischer Tropsch reaction, for the combustion of volatiles organic compounds [8, 9] as well as for other kinds of reactions because of their large specific areas and shape selective properties [10]. For its part, in view of their technological importance, the synthesis of magnetic systems with characteristic nanoscale dimensions has attracted much attention in the research field [11,

12]. Particularly, magnetic nanoparticles offer some attractive possibilities in biomedicine. One of the most important features of them is the possibility of controlling their size from a few nanometers up to tens of nanometers. Then, they reach dimensions comparable to those of biological entities allowing interacting with them, providing a controllable mean of tagging. In addition, the fact that the nanoparticles have magnetic properties opens the possibility to manipulate them with an external magnetic field gradient in order to make: delivering package such as anticancer drugs to a targeted region of the body such as a tumor, hyperthermia treatments, and magnetic resonance imaging contrast enhancements [13]. Meanwhile, the MCM-41 structure of mesoporous silicates, with a highly ordered structure of channels of well-defined size, is particularly suitable for the synthesis of nanospecies with magnetic properties. Bearing in mind the previous discussion, in this work we extend the study about Co nanospecies with magnetic properties loaded on MCM-41 silicates. Thus, the focus of this work is on its thorough identification, location and acidic properties in relation to their magnetic behavior through the application of specific spectroscopic techniques.

2 Experimental

2.1 Synthesis

The bare MCM-41 support was synthesized following the method already descript in our previous report [14] using cetyltrimethylammonium bromide (CTA) as template and tetraethoxysilane (TEOS) as silicon source. Then, the silicate matrix was modified with Co by the wet impregnation method using several concentrations of $Co(NO_3)_2 \cdot 6H_2O$ in aqueous solution in order to reach metal loadings of 1.0, 2.5, 5.0, 10.0 and 15.0 wt%. Then, water was evaporated and the solids calcined at 773 K for 9 h [15]. The calcined materials were designated as Co/M(x) where M indicates the presence of the MCM-41 structure and x indicates the nominal percentage of the metal loading.

2.2 Characterization

The Co content was determined by inductively coupled plasma optical emission spectroscopy (ICP) using an equipment VISTA-MPX CCD Simultaneus ICP-OES-VARIAN.

SEM micrographs were obtained in a JEOL model JSM 6380 LV. Gold coverage was applied to make samples conductive. The acceleration voltage was 20 kV. TEM images were obtained in a JEOL Model JEM-1200 EXII System, working voltage: 120 kV. A small drop of the dispersion (sample in water–ethanol 50% solution) was deposited on a copper grid and then evaporated in air at room temperature.

Co K-XANES/EXAFS spectra were acquired in transmission mode by using a Double Crystal Si(111) monochromator at the D08B-XAFS2 beamline of the LNLS (Campinas, Brazil) [16–20]. Powder samples were mixed with an appropriate amount of boron nitride and pressed into pellets. The incident photon energy was in the range of 7630–8700 eV with an energy resolution about 1.2 eV. The ionization chambers were filled with N_2/Ar_2 mixture under appropriate pressure for optimal absorption. For energy calibration purposes a Co metallic foil was placed between the second and the third ionization chamber. The photon energy was calibrated setting the first inflection point to the energy of the K absorption edge of metallic Co^0 (7709 eV). Data reduction was carried out with Demeter package programs [21].

X-ray photoelectron spectra (XPS) were carried out in a multi-technical system (SPECS) equipped with a dual X-ray source Mg/Al model XR50, which has a hemispheric analyzer PHOIBOS 150 operating in fix analyzer transmission mode (FAT). Spectra were acquired with pass energy of 30 eV, using Al anode operated at 100 W. Work pressure in analysis chamber was lower than 2.10^{-8} mbar. Binding energy values were corrected using as reference the adventitious C 1s line at 284.6 eV. The original XPS spectra were fitted by Gaussian curves using the conventional least squares method. Curve-fitting calculations were useful in determining each band location with confidence levels given by $R^2 \geq 0.99$.

FT-IR spectral measurements of pyridine adsorption on the samples were performed on a JASCO FT-IR 5300 spectrometer equipped with a DTGS detector. The range and resolution of acquisition data were $4600 - 400$ and 4 cm^{-1}, respectively. A self-supporting wafer for each sample (~20 mg and 13 mm of diameter) was prepared, placed in a thermostatted cell with CaF_2 windows connected to a vacuum line, and evacuated for 8 h at 673 K. The background spectrum was recorded first after cooling the sample to room temperature. Afterward, the solid wafer was exposed to pyridine vapors (Sintorgan, 99% purity) until the system was saturated to ~46 mmHg at room temperature; the contact time at this pressure was 12 h. The FT-IR spectrum for each sample was obtained after pyridine desorption by evacuation for 1 h at 473 or 573 K. All the spectra were recorded at room temperature before and after pyridine adsorption and desorption at each temperature.

The temperature dependence of the magnetization was measured following the conventional zero field cooling (ZFC) and the field cooling (FC) protocols, using a Quantum Design SQUID magnetometer MPMS XL7 with static field up to $\mu_0H = 10$ mT.

3 Results and discussion

The chemical composition and physical properties of all of the synthesized materials are shown in Table S1. A discussion of these data have been reported previously, and they are also added here in order to support the discussion presented in this report (see also Fig. S1) [15].

Then, TEM images of some Co/M(x) samples are shown in Fig. 1. As it can be observed, it could be confirmed the presence of the well-ordered parallel straight mesochannels, characteristic of the hexagonal pore arrangement, present in the samples. In this sense, the images of Fig. 1c, h are views perpendicular to the direction of the hexagonal pore arrangement, where the straight mesochannels arraying along the long axis are shown [22–24]. For its part, a frontal view of the pores can be observed in Fig. 1a, d, f, g, where the regular order of the channels is preserved without being affected by the presence of Co species. In agreement with these observations, the already reported XRD patterns for Co/M(x) samples (Fig. S2) [15] show that the mesoporous order

is sustained after the Co loading for all the metal contents. Moreover, no peaks corresponding to Co oxides appear in the high-angle XRD patterns (Fig. S3) for the lower Co loaded samples indicating that these species are amorphous or are clusters/particles too small to be detected by XRD. For its part, since the darker areas in TEM images represent the electronically more dense phases, metal oxide is considered to be present when irregular contrasts in the images are observed [25]. Thus, in Figs. 1g and 1h corresponding to samples with high Co loading, the incorporation of the cobalt oxide species inside the mesoporous channels could be confirmed. In fact, the impregnation with a high amount of Co nitrate followed by a calcination at 773 K, results in the formation of clusters or very small particles of oxide within the mesoporous silica channels evidenced by the darker regions along the mesopores [26].

The particle size and morphology of Co/M(x) samples were investigated by scanning electron microscopy. Figure 2 shows the SEM images of all of the samples. Here, particles with spherical-like morphology aggregated into larger

Fig. 1 Transmission electron microscopy images: (**a–b–c**) Co/M(1), (**d–e**) Co/M(2.5), (**f–g**) Co/M(5) and (**h**) Co/M(15)
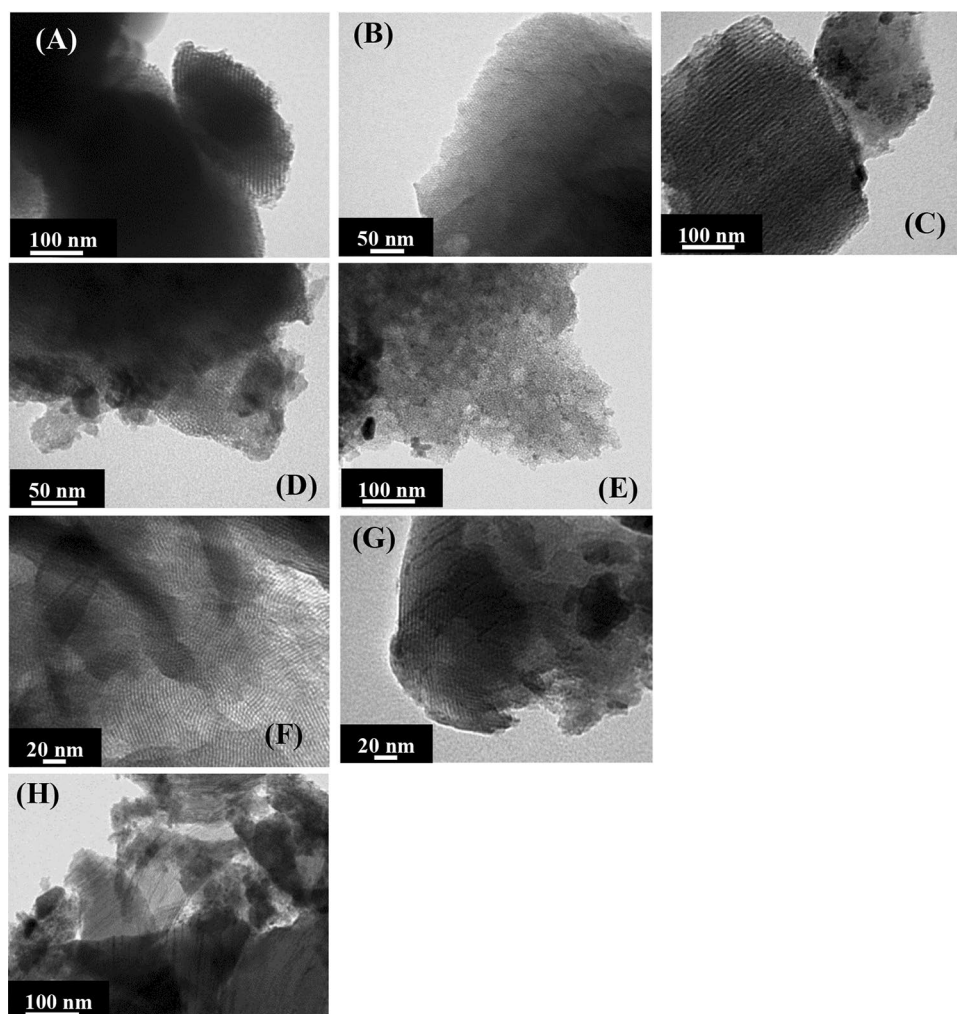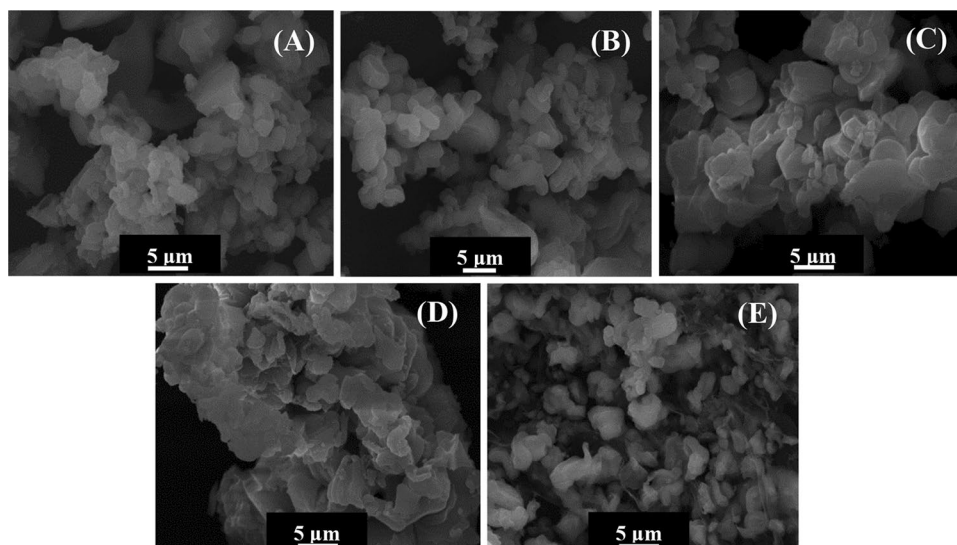
Fig. 2 Scanning electron microscopy images: **a** Co/M(1), **b** Co/M(2.5), **c** Co/M(5), **d** Co/M(10) and **e** Co/M(15)

secondary particles that exist in various morphologies and sizes could be observed [28–30].

This irregular morphology could be consequence of the metal oxides deposited on the silica matrix at several locations which provoke the agglomeration. This kind of morphology was already observed for MCM-41 silicates modified with Cr and Ti [27, 31].

In order to study the chemical state and relative abundance of the elements on the solid surface, photoelectron spectroscopy was used. Figure 3 illustrates the Co 2p region of the X-ray photoelectron spectra of Co/M(x) samples with nominal Co loadings from 1.0 to 15.0 wt%. As it could be observed, the Co2p transition splits into two peaks, 2p3/2 (780.5 eV) and 2p1/2 (795.4 eV) with a spin–orbit splitting of around 15.0 eV, which is in accordance with data reported in the literature [32–34].

Nevertheless, it is known that it is difficult to determine the Co cations oxidation states only from the binding energies (BE) of the Co2p main lines, because similar values can be obtained for most of the Co oxides and hydroxides (CoO, Co_2O_3, Co_3O_4, CoOOH). Then, satellite peak information should be considered. In this sense, it is generally accepted that energy gaps, between the Co2p main lines and the satellites peaks, are highly related to the oxidation states of Co cations. Thus, as it can be observed in Fig. 3, the relatively sharp peak width, the 2p1/2 to 2p3/2 separation of around 15 eV and the energy gaps between the main lines and their satellite peaks indicate the co-existence of Co^{2+} and Co^{3+} on the surface of the solids. For its part according to the literature, the two satellite peaks detected at about 6 eV (785.5 eV) and 9–10 eV (790 eV) above the Co2p3/2 main line could be assigned to Co cation valence of 2+ and 3+ present in the Co_3O_4 structure [35]. In this sense, the spectra of the samples synthesized in this work are similar to those corresponding to Co_3O_4 oxide, which has two types
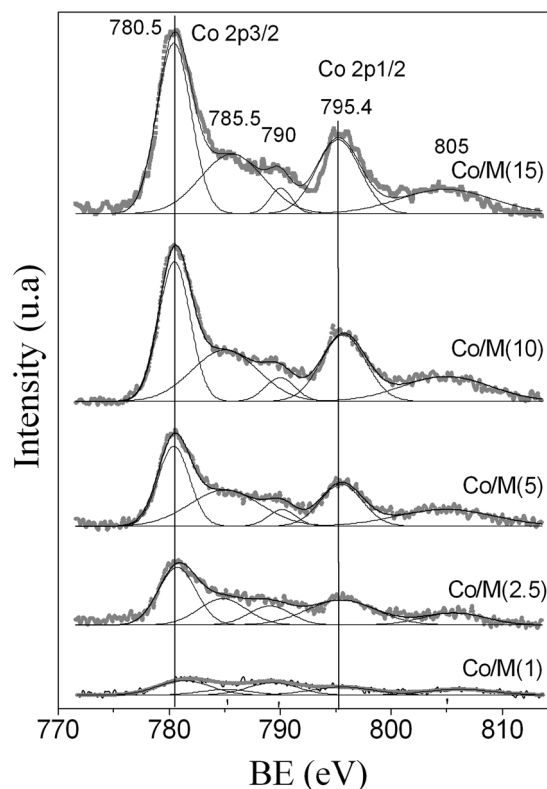

Fig. 3 Co 2p core level photoelectron profile of Co/M(x) samples

of Co ions, tetrahedral Co^{2+} and octahedral Co^{3+} [36].This behavior was already observed for materials calcined at high temperatures (higher than 673 K) where the weak satellites in the spectra were associated to the presence of the Co^{3+} ions in octahedral sites that exist in the spinel cobaltite structure formed onto the mesoporous silicate [36]. Therefore, the XPS technique allowed confirming the presence of Co oxide

in the form of Co_3O_4 already evidenced by UV–Vis DR [15]. It is important to note that, due to the low quantity of Co species in the surface (see Table 1), the characteristic Co 2p signals are hardly differentiable in the Co/M(1) sample.

On the other hand, for all of the synthesized solids, Table 1 lists the surface Co/Si atomic ratios determined by XPS and the bulk atomic Co/Si ratios determined by ICP. Generally, the surface Co/Si atomic ratio can be considered as the relative dispersion of transition metal ions on the structure of porous supports. In this sense, the values of this ratio were compared with the bulk Co/Si ratios [37]. For the Co/M(x) samples, the surface Co/Si atomic ratio increases with an increase in the bulk Co/Si ratio in the solids. Nevertheless, for all of the Co contents the surface Co/Si ratio is notably lower than the corresponding bulk Co/Si ratio, indicating that the Co atoms would be mostly incorporated inside the mesopores [26]. These results agree with the already observed by TEM analysis, where it could be observed the mesopores channels of the silica matrix filled with the Co oxide species.

Then, Fig. 4 shows the XPS spectra for the Si2p and O1s signals corresponding to the Co/M(15) sample taken as representative.

The Si2p BE of around 103.8 eV is characteristic of the MCM-41 silica. The XPS O1s spectra consist of two components with BE at around 530 and 533 eV corresponding to oxygen atoms from Co oxide species and from the silica support, respectively. As it can be observed in Table 1, the photoemission O1s for all of the Co/M(x) samples is mainly due to the contribution of oxygen from silica (higher than 90%). This fact would be other evidence of the presence of Co oxide species inside the mesoporous structure of the sieves. Nevertheless, a slight increase in the O1s percentage from the Co oxide species is observed with the metallic loading increasing which is according to the increased presence of the Co oxide species in the surface.

Co K-edge XAFS is a powerful tool for investigating the speciation and coordination structures of Co species formed in the silica mesoporous supports modified by the loading of this metal. Particularly, XANES spectra are frequently used as a "fingerprinting" to recognize a tetrahedral coordination

Table 1 XPS binding energy (BE) values and surface atomic concentration of Co/MCM-41 samples

Sample	Co[a] (wt%)	Co bulk (at.%)	Co/Si bulk	Co2p BE (eV)	Co[b] surface (at.%)	Co/Si surface	O 1s BE (eV) From Co_xO_y	O 1s BE (eV) From silica
Co/M(1)	0.80	0.27	0.008	780.5	0.14	0.004	530.2 (0.42)[c]	533.4 (99.58)[c]
Co/M(2.5)	2.20	0.76	0.023	779.6	0.29	0.009	530.2 (1.11)[c]	533.2 (98.89)[c]
Co/M(5)	4.35	1.52	0.046	779.9	0.46	0.015	530.5 (2.95)[c]	533.3 (97.05)[c]
Co/M(10)	8.81	3.17	0.098	780.2	1.29	0.039	530.4 (4.05)[c]	533.2 (95.94)[c]
Co/M(15)	11.90	4.38	0.137	780.2	1.92	0.060	530.4 (5.24)[c]	533.3 (94.75)[c]

[a]Determined by ICP

[b]Determined by XPS

[c]Between parenthesis the percentage composition of each species is shown

Fig. 4 XPS spectra of (**a**) Si 2p and (**b**) O 1 s for the Co/M(15) sample (taken as representative)
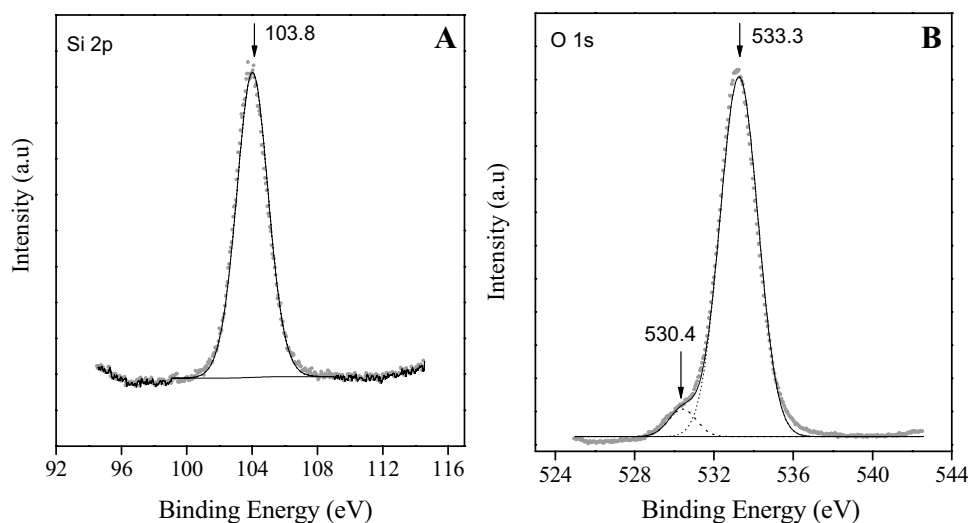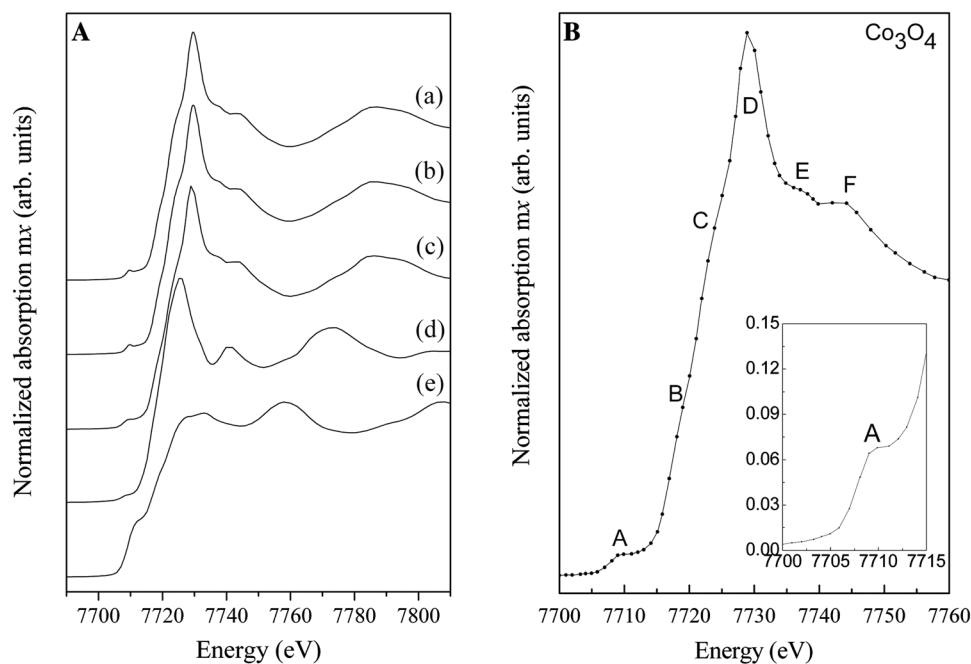
Fig. 5 A XANES spectra at the Co K edge for samples: (*a*) Co/M(5), (*b*) Co/M(10) and the following compounds used as references (*c*) Co3O4, (*d*) CoO and (*e*) Co0. **B** XANES spectra at the Co K edge for the Co3O4 oxide and a detail of their most important characteristics

from an octahedral one [38] and changes in the average oxidation states [39, 40]. Figure 5A shows the XANES spectra corresponding to the samples: Co/M(5) (a), Co/M(10) (b) and those from standards compounds used as references(c) Co_3O_4,(d) CoO and (e) metallic Co. Figure 5B shows the Co K XANES spectra corresponding to the Co_3O_4 with spinel structure. In this last figure, the A region (pre-edge region) is closely associated to the 3d electrons and to the symmetry. As it was mentioned before, it is known [41] that, at room temperature, the Co_3O_4 spinel has the presence of Co ions in tetrahedral and octahedral environments in a stoichiometric ratio of Co^{+2} $[Co^{+3}]_2O_4$, and that Co^{+2} from Co_3O_4 oxide, tetrahedrally coordinated by O^{2-} ions, is different from the octahedrally coordinated Co^{+2} present in CoO oxide [42].

For the standard spinel structure analyzed in this work, the A pre-edge peak is attributed to a dipolar forbidden transition 1s–3d characteristic of the tetrahedrally coordinated Co^{+2} [43], because this transition is forbidden when there is a reversal center in the metal cation, as it is the case of the non-distorted octahedrally coordination. Moreover, the pre-edge in the Co_3O_4 spectra is assigned to the presence of tetrahedrally coordinated Co^{+2} [44] due also to the peaks of this ion are more intense than those of octahedral Co^{+3}. This fact is due to the tetrahedral ligand field allows a dipolar transition, while in the octahedral symmetry, only a quadrupolar transition is allowed for 1s–3d [45].Another characteristic is that the pre-edge peak of the octahedral site is usually wider than the one corresponding to a tetrahedral site [44, 45]. According to the reported by T. Jiang and D.E. Ellis [46], the A pre-edge region corresponds to the transition 1s–3d already described, the shoulders B and C correspond

to contributions from multiple scattering in conjunction with the transition 1s–4s [44], the D peak corresponds to the allowed dipolar transition 1s–4p, and the resonances E and F correspond to contributions of multiple scattering. These are the main characteristics of the Co K XANES spectra of the spinel Co_3O_4 and, as it can be observed in Fig. 5A, the spectra of the two analyzed Co/M(x) samples are similar to that corresponding to the Co_3O_4 oxide. Then, as it was evidenced by the other techniques used here, the presence of Co_3O_4 spinel on the MCM-41 silicates could be confirmed.

Figure 6 shows the normalized EXAFS signals, $k^3\chi(k)$, and their corresponding Fourier transforms for Co/M(5), Co/M(10) and the standard Co_3O_4.

Particularly, Fig. 6F shows the features assigned to each maximum of the Fourier transform [47]. The first one corresponds to the Co–O coordination sphere, the second one to the Co(II)–Co(II) coordination sphere (tetrahedrally coordinated), and the third one to the Co(III)–Co(III) coordination sphere (octahedrally coordinated) [48]. By comparison with the signals corresponding to the standard Co_3O_4 oxide, the Co/M(x) samples analyzed in this work show a decrease in the intensity corresponding to $Co–Co(T_d)$, which is more notable for the sample Co/M(5), where there is also, a small variation in the intensity related to $Co–Co(O_h)$. This difference in the peak intensities (mainly for the lower loaded sample) with respect to the standard bulk oxide could be assigned to a certain disorder degree in the Co_3O_4 nanospecies present as clusters or nanoparticles of very small size, more finely dispersed and strongly interacting with the mesoporous matrix surface [48].
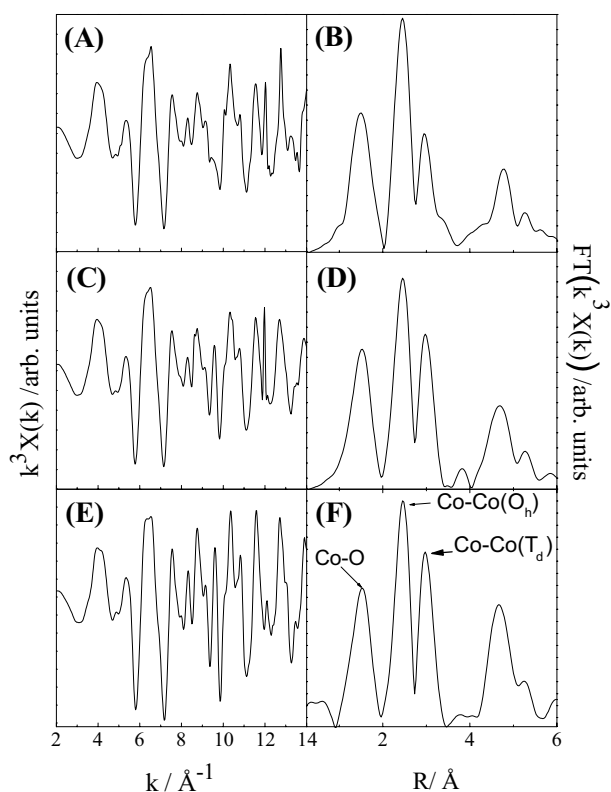
Fig. 6 EXAFS signal and their Fourier transform for sample (**a–b**) Co/M(5), (**c–d**) Co/M(10) and the standard (**e–f**) Co₃O₄

On the other hand, at higher metal loading, the segregation of the oxide nanospecies of bigger size with more defined crystalline structure is enhanced. This could be related to the fact that the presence of Co_3O_4 was evidenced by XRD for theoretical Co loadings of 10 and 15 wt% and not for the smaller metal loadings.

Then, the chemisorption of pyridine followed by FT-IR studies was used to detect the presence and nature of acid sites on the synthetized solids [49–52]. Figure 7 shows the FT-IR spectra of the Co/M(x) samples, recorded after the adsorption of pyridine and subsequent evacuation at 473 and 573 K. It is important to note that in order to make a semi quantitative and comparative analysis, all the curves were affected by the pellet mass. It is known that pyridine is a basic molecule that can interact with acid sites via the nitrogen lone-par electrons giving rise to different characteristic bands. Thus, these bands give information about the strength of Lewis and Brönsted acid sites. It can be observed that all samples show two bands at 1597 and 1447 cm⁻¹ corresponding to pyridine bonded to silanol groups whose hydroxyls are not capable of protonating pyridine [53–57]. These are the only bands found for the pure MCM-41 which disappear upon evacuation at 573 K indicating the weak interaction between pyridine and the Si–OH groups. For the Co containing solids, a band at 1610 cm⁻¹ corresponding to pyridine coordinately bonded to Lewis acid sites [50, 53, 56–60] could be observed, which is increasing proportionally with the Co loading. This band would be arising from the formation of a strong "electron–donor–acceptor" adduct between pyridine and Lewis sites, which result enough strong to retain pyridine even at 573 K. In addition, the systematic increase of the band at 1447 cm⁻¹ and its spectral shift towards higher wavenumber with the growing Co loading, could be interpreted in terms of the overlapping of
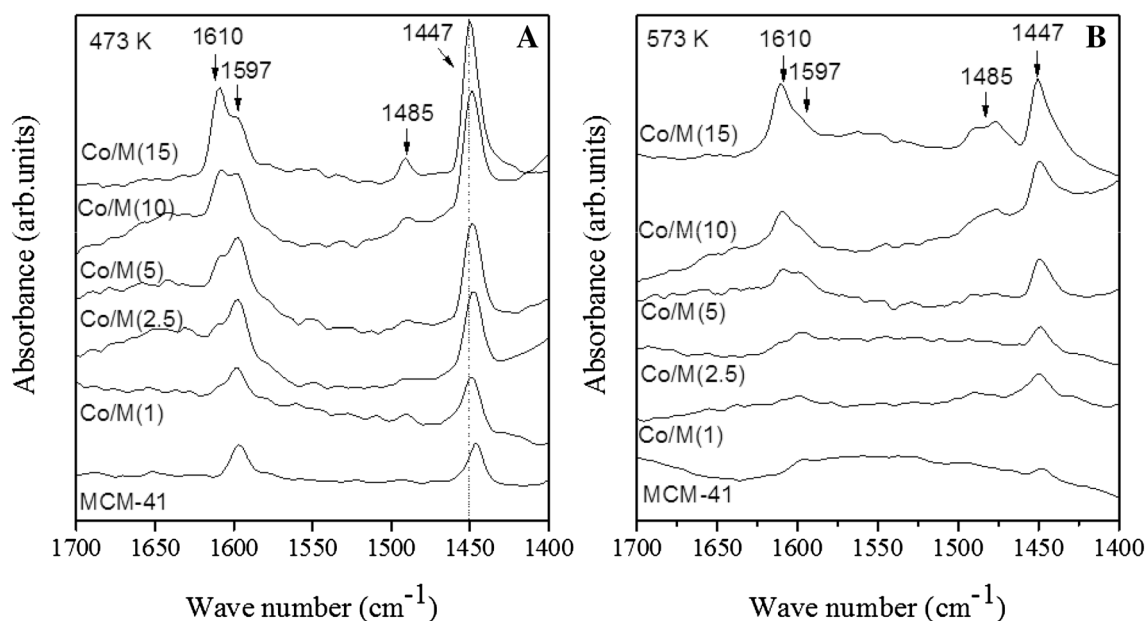

Fig. 7 FT-IR pyridine adsorbed on the samples Co/M(x) and the bare MCM-41 material after evacuation at: **a** 473 K and **b** 573 K

both the hydrogen-bonded pyridine band (1447 cm^{-1}) and a band attributed to the Lewis-type adduct which frequently appears at 1450 cm^{-1} [58]. In fact, the retention of this band until 573 K only for the Co/M(x) samples provides clear evidence that such band has a contribution from Lewis acid sites. Therefore, it is possible to suggest that the incorporation of Co in the siliceous matrix generates Lewis acid sites on the surface, which increase with the Co content. The origin of such Lewis acidity could arise from Co unoccupied molecular orbitals present in both the isolated Co species, coordinated to framework oxygen atoms in the channels, and the Co oxide species. Meanwhile, not all of the samples show bands at 1540 and 1636 cm^{-1} characteristic of Brönsted acid sites [60]. Therefore, the band observed at 1485 cm^{-1} in the Co/M(x) samples, frequently assigned to pyridine associated with both, Lewis and Brönsted acid sites, corresponds only to Lewis acid sites.

Considering the spectra of the samples in the hydroxyl range (Fig. 8), for samples with Co loading up to 5 wt%, it can be observed the presence of a band at 3740 cm^{-1} corresponding to the stretching vibrations of isolated terminal hydroxyl groups [26, 61–65].

Nevertheless, its decreased intensity with respect to the bare MCM-41 could be attributed to the condensation of some Si–OH groups with Co species leading to Si–O–Co bonds as well as to their partial blocking by the presence of some Co oxide clusters [66]. In addition, a broad contribution between 3700 and 3400 cm^{-1} that appears for the Co/M(x) samples with lower metal content could be assigned to the interaction between vicinal OH groups, as Si–OH and Co–OH groups [67]. Finally, the fact that the absorbance corresponding to the OH groups is strongly diminished
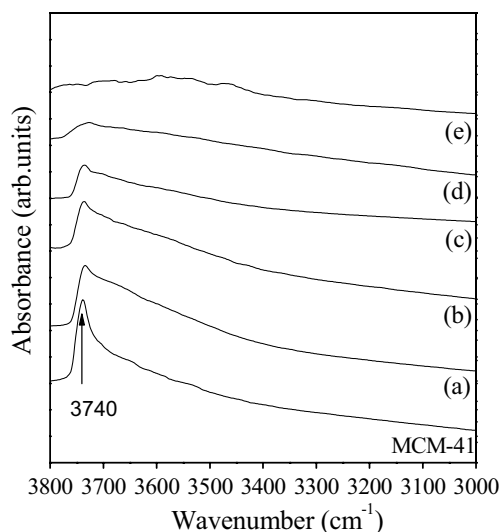
for the samples with higher Co content [Co/M(10) and Co/M(15)] is likely due to enhanced amount of oxide nanospecies which could be blocking the silanols, besides contributing to the Lewis acidity [68, 69].

In a previous report [15], the analysis of the curves of magnetization *vs* applied field, corresponding to the Co/M(x) samples, showed that the superparamagnetic contribution exhibit a maximum for a theoretical Co loading of 2.5 wt%. This behavior could be attributed to the presence of small Co nanospecies finely dispersed on the matrix. These species become larger for the higher Co loadings resulting in the decrease of the superparamagnetic contribution. In order to continue with this analysis, measurements of the temperature dependence of the magnetization were performed. Figure 9 shows the *zero-field-cooling* (ZFC) and *field-cooling* (FC) curves for the Co/M(2.5) sample, measured with an applied field of 0.01T. For this sample, a reversal behavior was observed for temperatures higher than ~150 K. Under this temperature, the magnetic system shows irreversibility with a maximum in the ZFC curve ($T_B = 4$ K), which is associated with a distribution in the blocking temperatures of nanoparticles of different size. Therefore, considering an Arrhenius type relaxation for non-interacting nanoparticles, the $<T_B>$ corresponds to the blocking of an average volume:

$$\ln \left(\tau_m / \tau_o \right) T_B k_B = KV$$

where K is the effective anisotropy constant, k_B is the Boltzmann constant, τ_m is the measure time ($\tau_m \sim 100$ s for SQUID measurements) and τ_o is the measurement time characteristic of the nanoparticles ($\tau_o \sim 10^{-11}$–10^{-9} s). Takada et al. [70] reported that superparamagnetic nanoparticles of Co$_3$O$_4$

Fig. 8 FT-IR spectra in the hydroxyl stretching region after degassing at 673 K for samples: (*a*) Co/M(1), (*b*) Co/M(2.5), (*c*) Co/M(5), (*d*) Co/M(10), (*e*) Co/M(15)
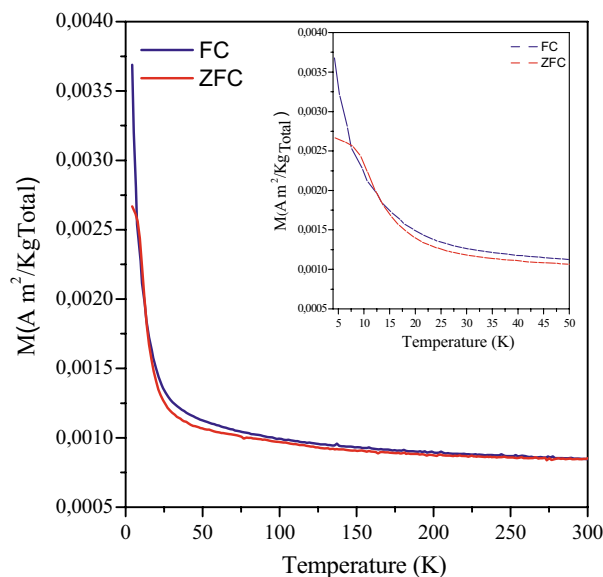

Fig. 9 Temperature dependence of the magnetization in the ZFC and FC states for an applied field for Co/M(2.5)

dispersed on amorphous SiO_2 matrix, with a size of around 3 nm, showed a T_B of 3.4 K and K of 9×10^5 erg cm^{-3}. In this sense, the T_B of around 4 K observed for the Co/M(2.5) sample (Fig. 9) allowed to infer a nanoparticle size consistent with the presence of Co_3O_4 inside the mesoporous of the MCM-41 matrix. This fact agrees with the statements arising from the results obtained by the other techniques. Considering the expected magnetic behavior in solids in order to be used in the controlled drug delivery systems a Co loading of 2.5 wt% lead to an adequate material for hosting drugs in their structure. Thus, an improved performance in the field of the controlled release of medicaments could be achieved.

4 Conclusions

Several specific spectroscopic techniques were carefully applied in order to infer on the nature and location of different Co species formed on MCM-41 mesoporous silicates by a fast post synthesis method. All the analyses evidenced the presence of Co oxide nanospecies inside the pores of the mesostructure. Thus, TEM images showed that the pores are filled with the Co species from the darker regions along the channels. Nevertheless, for the higher Co loadings, Co_3O_4 nanoparticles segregated on the external surface of the silicate were also observed. In accordance, XPS evidenced the co-existence of Co^{2+} and Co^{3+} on the surface of the solids which could be assigned to the spinel cobaltite structure (Co_3O_4) formed onto the mesoporous silicate. For all of the Co loadings, the surface Co/Si atomic ratios were notably lower than the corresponding bulk Co/Si ratios, indicating that the Co atoms are mostly incorporated inside the mesoporous channels of the silica matrix. In addition, comparing the XANES spectra of the Co/M(x) samples with some standard substances of Co, the presence of Co_3O_4 spinel on the MCM-41 silicates could be confirmed. With respect to the acidic properties of the synthesized materials, all of them showed a Lewis acidity increasing with the metal content. The presence of Lewis acid sites was assigned to both, the isolated Co species coordinated to framework oxygen atoms in the channels and Co oxide species. Finally, the results of the spectroscopic characterization and the presence of a T_B of around 4 K in the ZFC curve for the Co/M(2.5) sample, suggest that the Co oxide nanospecies of small size (clusters and Co_3O_4 nanoparticles) formed inside the MCM-41 mesopores are the responsible of notable superparamagnetic behavior. Such feature gives rise to solids with interesting properties for novel applications such as "drug hosting" for subsequent delivery through an external magnetic field. Therefore, these porous solids with improved performance result very promising in the field of the controlled release of medicaments.

References

1. A. Firouzi, S. Schaefer, B. Tolbert, G. Stucky, Chemelka magnetic-field-induced orientational ordering of alkaline lyotropic silicate—surfactant liquid crystals. J. Am. Chem. Soc. **119**, 9466–9477 (1997)
2. P. Yang, T. Deng, D. Zhao, P. Feng, D. Pine, B. Chemelka, G. Whitesides, G. Stucky, Hierarchically ordered oxides. Science **282**, 2244–2246 (1998)
3. C. Liang, Z. Li, S. Dai, Mesoporous carbon materials: synthesis and modification. Angew. Chem. **120**, 3754–3776 (2008)
4. S. Zhu, H. Zhou, T. Miyoshi, M. Hibino, I. Honma, M. Ichihara, Self-assembly of the mesoporous electrode material $Li_3Fe_2(PO_4)_3$ using a cationic surfactant as the template. Adv. Mater. **16**, 2012–2017 (2004)
5. Y. Zhang, S. Zha, M. Liu, Duale-scale porous electrodes for solid oxide fuels cells from polymer foams. Adv. Mater. **17**, 487–491 (2005)
6. L. Zhang, S. Qiao, Y. Jin, Z. Chen, H. Gu, G. Lu, Magnetic hollow spheres of periodic mesoporous organosilica and Fe_3O_4 nanocrystals: fabrication and structure control. Adv. Mater. **20**, 805–809 (2008)
7. K. Nam, D. Kim, P. Yoo, C. Chiang, N. Meethong, P. Hammond, Y. Chiang, A. Belcher, Virus-enabled synthesis and assembly of nanowires for lithium ion battery electrodes. Science **312**, 885–888 (2006)
8. R.J. Farrauto, C.H. Bartholomew, *Fundamental of Industrial Catalytic Processes* (Blackie Academic and Professional, London, 1997), pp. 640–644
9. J. Spivey, J. Butt, Literature review: deactivation of catalyst in the oxidation of volatile organic compounds. Catal. Today **11**, 465–500 (1992)
10. C. Dickinson, W. Zhou, R. Hodgkings, Y. Shi, D. Zhao, H. He, Formation mechanism of porous single-crystal Cr_2O_3 and Co_3O_4 templated by mesoporous silica. Chem. Mater. **18**, 3088–3095 (2006)
11. B. Barbara, Single particle nanomagnetism. Solid State Sci. **7**, 668–681 (2005)
12. K. Krishnan, A. Pakhomov, Y. Bao, P. Blomqvist, Y. Chun, M. Gonzales, K. Griffin, X. Ji, B. Roberts, Nanomagnetism and spin electronics: materials, microstructure and novel properties. J. Mater. Sci. **41**, 793–815 (2006)
13. Q. Pankhurst, J. Commolly, S. Jones, J. Dobson, Applications of magnetic nanoparticles in biomedicine. J. Phys. D **36**, 167–181 (2003)
14. V. Elías;, M. Crivello, E. Herrero, S. Casuscelli, G. Eimer, Some considerations to optimize the synthesis procedure and the structural quality of mesostructured silicas. J. Non-Cryst. Solids **355**, 1269–1273 (2009)
15. N. Cuello, V. Elías, M. Crivello, M. Oliva, G. Eimer, Synthesis, characterization and magnetic behavior of Co/MCM-41 nanocomposites. J. Solid State Chem. **205**, 91–96 (2013)
16. http://www.rigaku.com/xas/rxas.html
17. http://nano.fisica.unlp.edu.ar/facilities.php
18. A. Thenon, M. Mizrahi, L. Andrini, L. Giovanetti, J. Ramallo-López, F. Requejo, Comisionamiento del espectrómetro de absorción de rayos-X in house R-XAS Looper de RIGAKU, 21ª RAU, Campinas, SP, Brasil (22 and 23 de february 2011)

19. K. Shinoda, S. Zuzuki, M. Kuribayasi, T. Tasguchi, J. Phys. **186**, 012036 (2009)
20. http://lnls.cnpem.br/beamlines/xafs/beamlines/xafs2/
21. http://bruceravel.github.io/demeter/
22. K. Choi, R. Wakabayashi, T. Tatsumi, T. Yokoi, K. Kuroda, Usefulness of alkoxyltitanosiloxane for the preparation of mesoporous silica containing a large amount of isolated titanium. J. Colloid Interface Sci. **359**, 240–247 (2011)
23. Y. Xu, G. Zhou, C. Wu, T. Li, H. Song, Improving adsorption and activation of the lipase immobilized in amino-functionalized ordered mesoporous SBA-15. Solid State Sci. **13**, 867–874 (2011)
24. A. Patterson, The Scherrer formula for X-ray particle size determination. Phys. Rev. **56**, 978–982 (1939)
25. I. Park, J. Ha, J. Khim, Synthesis and characterization of visible-light absorbing ordered mesoporous titanosilicate incorporated with vanadium oxide. Chem. Phys. Lett. **444**, 161–166 (2007)
26. M. Moreno, M. Weyland, P. Midgley, J. Bengoa, M. Cagnoli, N. Gallegos, A. Alvarez, S. Marchetti, One-template synthesis of Ti-Al-containig mesoporous silicas and the application as potential photocatalytic degradation of chlorophenols. Micron **37**, 52–56 (2006)
27. V. Elías, E. Sabre, E. Winkler, M. Satuf, E. Rodriguez-Castellón, S. Casuscelli, G. Eimer, Chromium and titanium/chromium-containing MCM-41 mesoporous silicates as promising catalystd for the photobleaching of azo dyes in aqueous suspensions. A multitechnique investigation. Microporous Mesoporous Mater. **163**, 85–95 (2012)
28. X. Hao, Y. Zhang, J. Wang, W. Zhou, C. Zhang, S. Liu, A novel approach to prepare MCM-41 supported CuO catalyst with high metal loading and dispersion. Microporous Mesoporous Mater. **88**, 38–47 (2006)
29. T. Tsoncheva, S. Areva, M. Dimitrov, D. Paneva, I. Mitov, M. Linden, C. Minchev, MCM-41 silica modified with copper and iron oxides as catalysts for methanol decomposition. J. Mol. Catal. A. **1–2 246**, 118–127 (2006)
30. D. Yin, W. Li, W. Yang, H. Xiang, Y. Sun, B. Zhong, S. Peng, Mesoporous HMS molecular sieves supported cobalt catalyst for Fischer Tropsch synthesis. Microporous Mesoporous Mater. **47**, 15–24 (2001)
31. V. Elías;, E. Sabre, K. Sapag, S. Casuscelli, G. Eimer, Influence of the Cr loading in Cr/MCM-41 and TiO2/Cr/MCM-41 molecular sieves for the photodegradation of Acid Orange 7. Appl. Catal. A. **413–414**, 280–291 (2012)
32. J. Marco, J. Gancedo, M. Gracia, J. Gautier, E. Ríos;, H. Palmer, C. Greaves, F. Berry, Cation distribution and magnetic structure of the ferrimagnetic spinel $NiCo_2O_4$. J. Mater. Chem. **11**, 3087–3093 (2001)
33. T. Baird, K. Campbell, P. Hollimen, R. Hoyle, M. Huxam, D. Stirling, B. Williams, M. Morris, Cobalt-zinc oxide absorbents for low temperature gas desulfurization. J. Mater. Chem. **9**, 599–605 (1999)
34. J. Marco, J. Gancedo, M. Gracia, J. Gautier, E. Ríos, F. Berry, Characterization of Niquel Cobaltite $NiCo_2O_4$ Prepared by several methods: an XRD, XANES, EXAFS and XPS study. J. Solid State Chem. **153**, 74–81 (2000)
35. B. Ernst, S. Libst, P. Chaumette, A. Kiennemann, Rock salt-spinel structural transformation in anodically electrodeposited Mn-Co-O nanocrystals. Appl. Catal. A **186**, 145–168 (1999)
36. Y. Feng, L. Li, S. Niu, Y. Qu, Q. Zhang, Y. Li, W. Zhao, H. Li, J. Shi, Controlled synthesis of highly active mesoporous Co_3O_4 polycristals for low temperature CO oxidation. Appl. Catal. B **111–112**, 461–466 (2012)
37. S. Shylesh, P. Samuel, A. Singh, Appl. Catal. A **318**, 128–136 (2007)
38. A. Mottana, J. Robert, A. Marcelli, G. Giuli, G. Della Ventura, E. Paris, Z. Wu, Octahedral versus tetrahedral coordination of Al in synthetic micas determined by XANES. Am. Mineral. **82** 497–502 (1997)
39. T. Capehart, J. Herbst, R. Mishra, F. Pinkerton, X-ray-absorption edge shifts in rare-earth-transition-metal compounds. Phys. Rev. B **52**, 7907–7914 (1995)
40. C. Engemann, J. Hormes, A. Longen, K. Dötz, An X-ray absorption near edge spectroscopy XANES study on organochromium complexes at the Cr K-edge. Chem. Phys. **237**, 471–481 (1998)
41. X. Liu, C. Prewitt, High-temperature X-ray diffraction study of Co_3O_4: transition from normal to disordered spinel. Phys. Chem. Miner. **17**, 168–172 (1990)
42. M. Lelis, A. Porto, C. Gonçalves, J. Fabris, Cation occupancy sites in synthetic Co-doped magnetites as determined with X-ray absorption (XAS) and Mössbauer spectroscopies. J. Magn. Magn. Mater. **278**, 263–269 (2004)
43. A. Serrano, E. Fernandez Pinel, A. Quesada, I. Lorite, M. Plaza, L. Pérez, F. Jiménez-Villacorta, J. de la Venta, M. Martín-González, J. Costa-Krämer, J. Fernandez, J. Llopis, M. García, Room-temperature ferromagnetism in the mixtures of the TiO_2 and Co_3O_4 powders. Phys. Rev. B **79**(1–5), 144405 (2009)
44. L. Bai, M. Pravica, Y. Zhao, C. Park, Y. Meng, S. Sinogeikin, G. Shen, Charge transfer in spinel Co_3O_4 at high pressures. J. Phys. **24**(1–7), 435401 (2012)
45. T. Yamamoto, Assignment of pre-edge peaks in K-edge X-ray absorption spectra of 3d transition metal compounds: electric dipole or quadrupole. X-Ray Spectrum. **37**, 572–584 (2008)
46. T. Jiang, D. Ellis, X-ray absorption near edge structures in cobalt oxides. J. Mater. Res. **11**, 2242–2256 (1996)
47. N. Koizumi, S. Suzuki, Y. Ibi, Y. Hayasaka, Y. Hamabe, T. Shindo, M. Yamada, J. Synch, Mechanism for enhancing dispersion of Co_3O_4 nanoparticles in Co/SiO_2 Fischer-Tropsch synthesis catalyst by adding glycol to impregnating solution: a quick-XAFS study. Rad **19**, 74–83 (2012)
48. M. Ma, Z. Pan, W. Wang, L. Guo, J. Li, Z. Wu, S. Yang, Microstructure and gas-sensing property of the ordered mesoporous Co_3O_4. J. Nanosci. Nanotechnol. **13**, 864–868 (2013)
49. C. Chanquía, L. Andrini, J. Fernández, M. Crivello, F. Requejo, E. Herrero, G. Eimer, Speciation of copper in spherical mesoporous silicates: from the Microscale to Angstrom. J. Phys. Chem. C **114**, 12221–12229 (2010)
50. B. Chakraborty, B. Viswanathan, Surface acidity of MCM-41 by in situ IR studies of pyridine adsorption. Catal. Today **49**, 253–260 (1999)
51. M. Hunger, U. Schenk, M. Breuninger, R. Gläser, J. Weitkamp, Characterization of the acid sites in MCM-41-type materials by spectroscopic and catalytic techniques. Microporous Mesoporous Mater. **27**, 261–271 (1999)
52. X. Zhao, G. Lu, A. Whittaker, G. Millar, H. Zhu, Comprehensive study of surface chemistry of MCM-41 Using ^{29}Si CP/MAS NMR, FTIR, Pyridine-TPD, and TGA. J. Phys. Chem. B **101**, 6525–6531 (1997)
53. T. Conesa, J. Hidalgo, R. Luque, J. Campelo, A. Romero, Influence of the acid-base properties in Si-MCM-41 and B-MCM-41mesoporous materials on the activity and selectivity of e-caprolactam synthesis. Appl. Catal. A **299**, 224–234 (2006)
54. A. Jentys, K. Kleestorfer, H. Vinek, Concentration of surface hydroxyl groups on MCM-41. Microporous Mesoporous Mater. **27**, 321–328 (1999)
55. G. Eimer, S. Casuscelli, C. Chanquia, V. Elías, M. Crivello, E. Herrero, The influence of Ti-loading on the acid behavior and on the catalytic efficiency of mesoporous Ti-MCM-41 molecular sieves. Catal. Today **133**, 639–646 (2008)
56. D. Trong, S. Nguyen, V. Hulea, E. Dumitriu, S. Kaliaguine, Mono- and bifunctional MFI, BEA and MCM-41 titanium-molecular sieves. Part 1. Synthesis and characterization. Microporous Mesoporous Mater. **57**, 169–180 (2003)

57. D. Srinivas, R. Srivastava, P. Ratnasamy, Transesterifications over titanosilicate molecular sieves. Catal. Today **96**, 127–133 (2004)

58. A. Sakthivel, S. Dapurkar, N. Gupta, S. Kulshreshtha, P. Selvam, The influence of aluminium sources on the acidic behavior as well as on the catalytic activity of mesoporous H-AlMCM-41 molecular sieves. Microporous Mesoporous Mater. **65**, 177–187 (2003)

59. C. Otero, M. Areán, V. Rodríguez Delgado, J. Montouillout, C. Lavalley, J. Fenández, J. Cuart Pascual, Parra, NMR and FTIR spectroscopic studies on the acidity of gallia-silica prepared by a sol-gel route. Microporous Mesoporous Mater. **67**, 259–264 (2004)

60. L. Cedeño, D. Hernández, T. Klimova, J. Ramírez, Synthesis of Nb-containing mesoporous silica molecular sieves Analysis of its potential use in HDS catalysts. Appl. Catal. A **241**, 39–50 (2003)

61. F. Gao, Y. Zhang, H. Wan, Y. Kong, X. Wu, L. Dong, B. Li, Y. Chen, The states of vanadium species in V-SBA-15 synthesized under different pH values. Microporous Mesoporous Mater. **110**, 508–516 (2008)

62. Y. Segura, P. Cool, P. Kustroeski, L. Chmielarz, R. Dziembaj, E. Vansant, Characterization of vanadium and titanium oxide supported SBA-15. J. Phys. Chem. B **109**, 12071–12079 (2005)

63. M. Anpo, M. Matsuoka, Y. Shioya, H. Yamashita, E. Gimello, C. Monterra, M. Che, H. Patterson, S. Webber, S. Ouellette, M. Fox, Preparation and characterization of the Cu+/ZSM-5 catalyst and its reaction with NO under UV irradiation at 275 K. In situ photoluminescence, EPR, and FT-IR investigations. J. Phys. Chem. **98**, 5744–5750 (1994)

64. L. Chmielarz, P. Kustrowski, R. Dziembaj, P. Cool, E. Vansant, Catalytic performance of various mesoporous silicas modified with copper or iron oxides introduced by different ways in the selective reduction of NO by ammonia. Appl. Catal. B **62**, 369–380 (1994)

65. I. Babich, Y. Plyuto, P. Van der Voort, E. Vansant, Thermal transformations of chromium acetylacetonate on silica surface. J. Colloid Interface Sci. **189**, 144–150 (1997)

66. P. Carraro, V. Elías, A. García Blanco, K. Sapag, S. Moreno, M. Oliva, G. Eimer, Synthesis and multi-technique characterization of nickel loaded MCM-41 as potential hydrogen-storage materials. Microporous Mesoporous Mater. **191**, 103–111 (2014)

67. M. Tamura, W. Chaikittisilp, T. Yokoi, T. Okubo, Incorporation process of Ti species into the framework of MFI type zeolite. Microprorous Mesoporous Mater. **112**, 202–210 (2008)

68. L. Pierella, C. Saux, H. Bertorello, P. Bercoff, P. Botta, J. Rivas, Occluded cobalt species over ZSM-5 matrix: design, preparation, characterization and magnetic behavior. Mater. Res. Bull **43**, 2026–2035 (2008)

69. D. Dumitriu, R. Barjega, L. Frunza, D. Macovei, T. Hu, Y. Xie, V. Parvulescu, S. Kaliaguine, BiOx clusters occluded in a ZSM-5 matrix: preparation, characterization, and catalytic behavior in liquid-phase oxidation of hydrocarbons. J. Catal. **219**, 337–351 (2003)

70. S. Takada, M. Fujii, S. Kohiki, T. Babasaki, H. Deguchi, M. Mitome, M. Oku, Intraparticle magnetic properties of Co_3O_4 nanocrystals. Nano Lett. **1**, 379–382 (2001)